PAPER

Check for updates

Lithium-ion batteries with fluorinated mesogen-based liquid-crystalline electrolytes: molecular design towards enhancing oxidation stability†

Shingo Takegawa, [ID] [a] Kazuma Hamaguchi,[a] Eiji Hosono, [ID] [b] Shunsuke Sato,[c] Go Watanabe, [ID] [c,d,e] Junya Uchida [ID] [a] and Takashi Kato ⋆[a,f]

Two-dimensional (2D) nanostructured liquid crystals containing fluorinated cyclohexylphenyl and cyclic carbonate moieties have been developed as quasi-solid-state self-organized electrolytes for safe lithium-ion batteries. We have designed lithium ion-conductive liquid-crystalline (LC) materials with fluorine substituents on mesogens for improved oxidation stability. Computational studies suggest that the fluorination of mesogens lowers the highest occupied molecular orbital (HOMO) level of LC molecules and improves their oxidation resistance as electrolytes. The LC molecule complexed with lithium bis(trifluoromethanesulfonyl)imide exhibits smectic A LC phases with 2D ion transport pathways over wide temperature ranges. Cyclic voltammetry measurements of the fluorinated mesogen-based LC electrolytes indicate that they are electrochemically stable above 4.0 V *vs.* Li/Li$^+$. Lithium half-cells composed of fluorinated LC electrolytes show higher discharge capacity and coulombic efficiency than those containing non-fluorinated analogous LC molecules. Combining molecular dynamics simulations with the experimental results, it is revealed that the fluorination of the mesogen effectively enhances the electrochemical stability of the LC electrolytes without significantly disrupting ionic conductivities and the LC order.

Introduction

Nanostructured liquid-crystalline (LC) materials[1–10] have attracted considerable attention as transport materials for ions,[1–3,5,6,11–26] electrons,[1,2,6–8,27–31] and molecules[1,4,9,32–39] because they form well-organized molecular-based nanostructures for potential applications in energy, environment, resources, and separation materials. LC molecules having block structures consisting of incompatible moieties form nanosegregated structures. The transport pathways formed by nanosegregation are expected to enable the efficient transport

of ions, electrons, or molecules even in quasi-solid states. The dynamic and soft properties of LC materials also contribute to switching,[1–4,6,10,23,37] flexibility,[1–10,16,21] processability,[1,2,8,27,31] or interfacial compatibility.[2,3,8,21]

The aim of this study is to develop nanostructured LC electrolytes for lithium-ion batteries (Fig. 1). We successfully prepared lithium-ion batteries with an LC electrolyte for the first time using a smectic rod-like LC molecule complexed with a lithium salt.[11] This LC electrolyte showed a smectic phase to construct two-dimensional (2D) ion-conduction pathways. Ionic conductivities in the order of 10^{-6}–10^{-4} S cm^{-1} were achieved with these LC electrolytes in the quasi-solid states. These LC molecules need to be designed to meet the requirements for lithium-ion battery operations including electrochemical stability.

Conventional electrolytes for lithium-ion batteries consist of organic low-molecular-weight carbonates which have inherent safety issues, such as leakage, volatility, and flammability.[40–42] To ensure the safety of lithium-ion batteries, various electrolytes, such as solid inorganic electrolytes,[43–46] solid polymer electrolytes,[43,47–52] gel polymer electrolytes,[53] or ionic liquid electrolytes,[54] have been studied. Solid inorganic electrolytes, represented by oxides, have ordered structures and exhibit high ionic conductivities; however, they experience high resistance at grain boundaries or instability with lithium metal anodes.[43,44] Polymer electrolytes are promising candi-

[a]*Department of Chemistry and Biotechnology, School of Engineering, The University of Tokyo, 7-3-1 Hongo, Bunkyo-ku, Tokyo 113-8656, Japan.*
E-mail: kato@chiral.t.u-tokyo.ac.jp
[b]*Global Zero Emission Research Center, National Institute of Advanced Industrial Science and Technology (AIST), 16-1 Onogawa, Tsukuba, Ibaraki 305-8569, Japan*
[c]*Department of Physics, School of Science, Kitasato University, 1-15-1 Kitazato, Minami-ku, Sagamihara, Kanagawa 252-0373, Japan*
[d]*Department of Data Science, School of Frontier Engineering, Kitasato University, 1-15-1 Kitazato, Minami-ku, Sagamihara, Kanagawa 252-0373, Japan*
[e]*Kanagawa Institute of Industrial Science and Technology (KISTEC), 705-1 Shimoimaizumi, Ebina, Kanagawa 242-0435, Japan*
[f]*Institute for Aqua Regeneration, Shinshu University, 4-17-1 Wakasato, Nagano 380-8553, Japan*
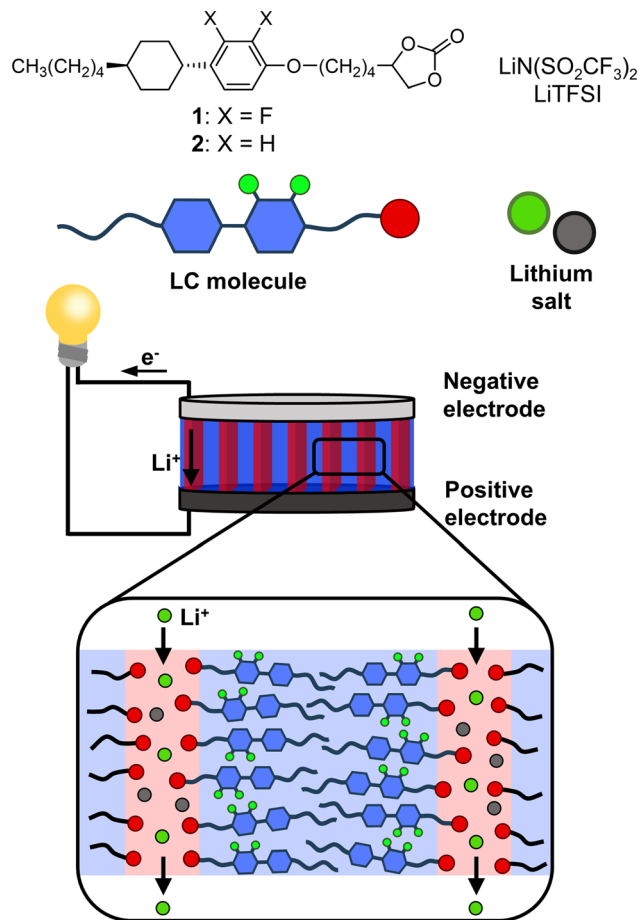†Electronic supplementary information (ESI) available. See DOI: https://doi.org/10.1039/d4nr03559c

Fig. 1 Schematic illustration of the lithium-ion battery containing the LC electrolytes in the ideal state.

dates owing to their lightness, processability, and flexibility; however, the ionic conductivities in the amorphous region are relatively lower.[43,47,48] Nanostructured ion-conductive liquid crystals[1–3,5,6,11–23] also show potential as quasi-solid electrolytes because they provide dynamic ordered structures, which may contribute to safety, good compatibility with electrodes, and efficient ion transport through self-assembly pathways. Furthermore, it was reported that ordered LC structures could effectively suppress the growth of lithium dendrites which cause capacity fading and short circuits, hindering the practical application of lithium metal anodes.[18–21]

In the present study, we focus on the fluorination of aromatic mesogens as a new approach for the enhancement of the oxidation resistance of LC electrolytes. The electrochemical stability of electrolytes is an important factor determining the efficiency and cyclability of batteries.[55–57] Fluorine atoms are characterized by small volume, high electronegativity, low polarizability, and the formation of stable C–F bonds. Associated with the nature of fluorine atoms, fluorinated organic electrolytes[49–52,58–65] possess superior electrochemical and physicochemical properties, such as higher oxidation stability,[49–52,58–65] nonflammability,[58,59,63–65] and low-tempera-

ture performance.[58,59,64] Conversely, the physicochemical and LC properties of a variety of fluorinated liquid crystals[14,17,66–72] have been reported. Fluorinated liquid crystals have often been studied for display applications that modulate their physicochemical properties.[66–71]

Herein, we report the effects of fluorination of LC molecules on the electrochemical and self-assembly properties of compound **1**. The performance of lithium-ion batteries based on the LC electrolytes of **1** and lithium salts using half-cells comprising LiFePO$_4$, Li metal, and LC electrolytes is described.

Results and discussion

Compound **1** has a fluorinated rod-like mesogen and a cyclic carbonate group at the extremities of the alkyl spacer (Fig. 1). Compound **1** is a fluorinated analogue of compound **2**. Compound **2** complexed with a lithium salt was previously used as an LC electrolyte for lithium-ion battery studies.[11] However, the cells with compound **2** based LC electrolytes were reported to deteriorate gradually in repeated charge–discharge reactions due to the insufficient oxidation resistance of compound **2**.[11,12] Fluorine substituents were introduced to the lateral part of the mesogen to enhance the oxidation resistance. We expected that the electron-withdrawing fluorine atoms would stabilize the highest occupied molecular orbital (HOMO), which is localized at the cyclohexylphenyl moiety. The density functional theory (DFT) calculations (B3LYP/6-31G (d), Spartan'18) confirmed that compound **1** has a HOMO level of −6.07 eV, which is lower than that of compound **2** (Fig. 2). The stabilization of the HOMO was envisioned to result in the enhanced oxidation resistance of the LC electrolytes and stable charge–discharge reactions. From a view of self-assembling properties, complexes of compound **1** and lithium salts were expected to form 2D ion-conduction pathways where the lithium ions should interact with the carbonate moieties,[11,12,15,17] such as compound **2**. Due to the wider 2D pathways of the smectic phases, the conduction pathways would be partially connected, even in polydomain states.[11–13,38] The laterally fluorinated mesogens may suppress excessive intermolecular packing that decreases conductivity and compatibility with electrodes.[66,69,73]

Compound **1** was synthesized from commercially available 1-ethoxy-2,3-difluoro-4-(*trans*-4-pentylcyclohexyl)benzene as the starting material (Scheme S1†). Compound **1** was characterized by ^{1}H and ^{13}C nuclear magnetic resonance spectroscopy, matrix-assisted laser desorption ionization time-of-flight mass spectrometry, and elemental analysis (Fig. S1 and S2†).

The LC properties of compound **1** were studied by differential scanning calorimetry (DSC), polarized optical microscopy (POM), and X-ray diffraction (XRD) measurements (Table 1, Fig. S3–S5†). Compound **1** showed an enantiotropic smectic A (SmA) phase with an isotropization temperature of 65 °C. No LC phases other than the SmA phase were observed for compound **1** when cooled to −20 °C. Compound **1** did not exhibit a smectic B (SmB) phase, while compound **2** exhibited an SmB
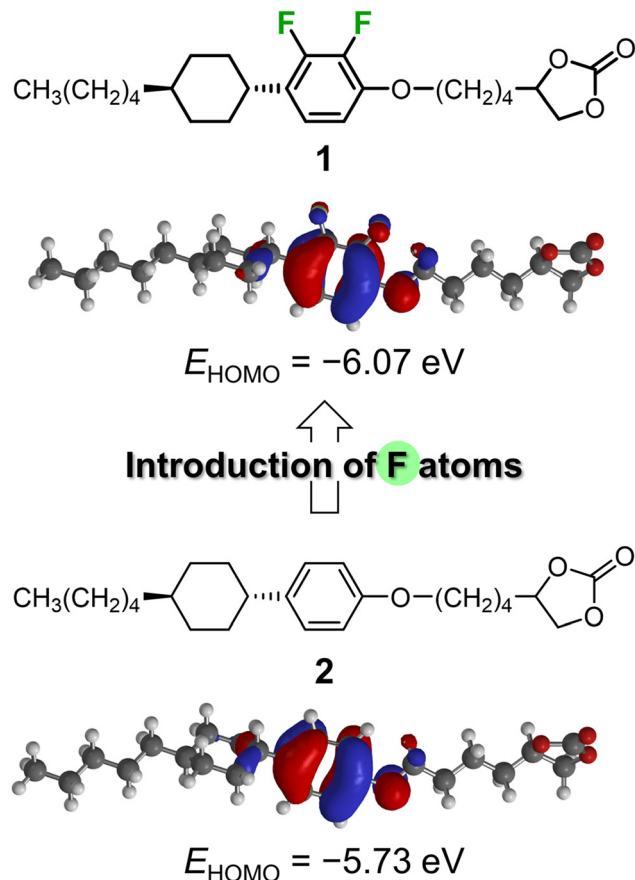
Fig. 2 Molecular structures, HOMO structures and HOMO energy levels (DFT, B3LYP/6-31G(d), Spartan'18) of the compounds: compound **1** with a fluorinated cyclohexylphenyl mesogen and compound **2** consisting of a non-fluorinated cyclohexylphenyl mesogen.

Table 1 Phase transition behavior of compounds **1** and **2**

Compound	Phase transition behavior[a]				
1	Iso	65	SmA		
2 [b]	Iso	96	SmA	22	SmB

[a] Phase transition temperature (°C) determined by DSC during the cooling process. Scanning rate: 10 °C min⁻¹. [b] Ref. 11. Iso: isotropic; SmA: smectic A; and SmB: smectic B.

phase as well as an SmA phase.[11] The fluorine atoms of compound **1** may disturb the ordered packing of mesogens in the layer plane.[66,69,73] The effects of the lateral fluorine substituents on liquid crystallinity will be discussed later in combination with molecular dynamics simulations.

Complexes of **1**/lithium bis(trifluoromethanesulfonyl)imide (LiTFSI) were prepared at molar ratios of 90 : 10, 80 : 20, 70 : 30, and 60 : 40. The interactions between **1** and LiTFSI were examined using Fourier transform infrared (FT-IR) spectroscopy (Fig. 3 and S6†). Compound **1** showed a characteristic stretching vibrational band due to the C=O group in the cyclic carbonate moiety at 1796 cm⁻¹ at 30 °C. Upon addition of LiTFSI,
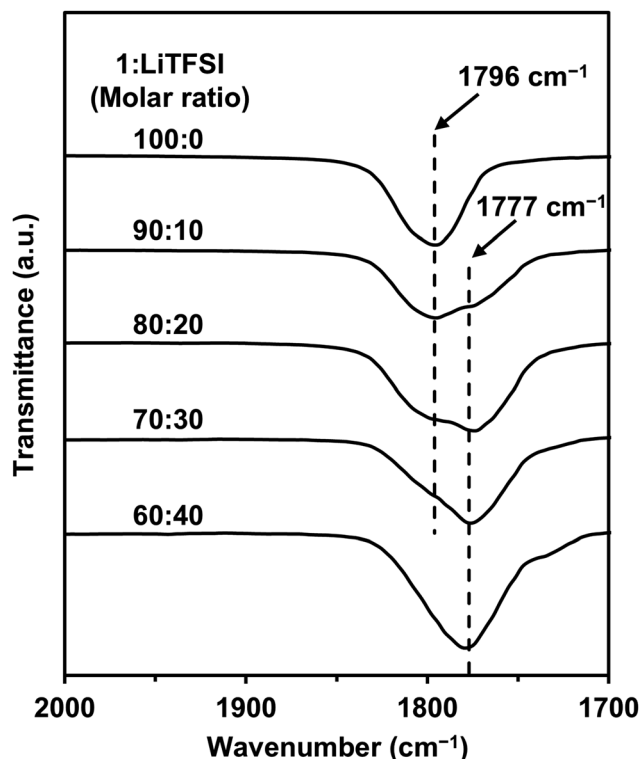

Fig. 3 FT-IR spectra of **1**/LiTFSI complexes in the SmA phases at 30 °C.

the band of the C=O stretching vibration of the cyclic carbonate coordinated to lithium ions was observed at 1777 cm⁻¹. These observations supported the hypothesis that **1** and LiTFSI formed complexes. These band shifts derived from the interactions between lithium ions and the C=O group have also been reported for complexes **2**/LiTFSI.[15]

Fig. 4a shows a phase diagram of **1**/LiTFSI complexes (Fig. S7 and S8†). The **1**/LiTFSI complex at a molar ratio of 80 : 20 showed a homeotropic alignment in the SmA phase, which was confirmed by the dark POM image and the cross pattern of the conoscopic image (Fig. 4b). The XRD pattern of the **1**/LiTFSI complex at a molar ratio of 80 : 20 at 60 °C shows the formation of a layered structure with a *d*-spacing of approximately 44 Å (Fig. 4c). A diffusion halo is observed in the wide-angle region. Considering the molecular length of compound **1** (23 Å) obtained by structural optimization using DFT, these results suggest the formation of the SmA phase with a bilayer structure (Fig. 5). The isotropization temperatures of **1**/LiTFSI complexes were higher than that of compound **1** (Fig. 4a). The nanosegregated layered assemblies in the SmA phases were stabilized by ion–dipole interactions between the polar carbonate moieties of **1** and the lithium ions, as observed from the FT-IR measurements. The isotropization temperature of **1**/LiTFSI at a molar ratio of 60 : 40 was lower than that at 70 : 30, resulting from the destabilization of the layered structures by the bulky TFSI anions.

The ionic conductivities of **1**/LiTFSI complexes were measured by an alternative current impedance method using
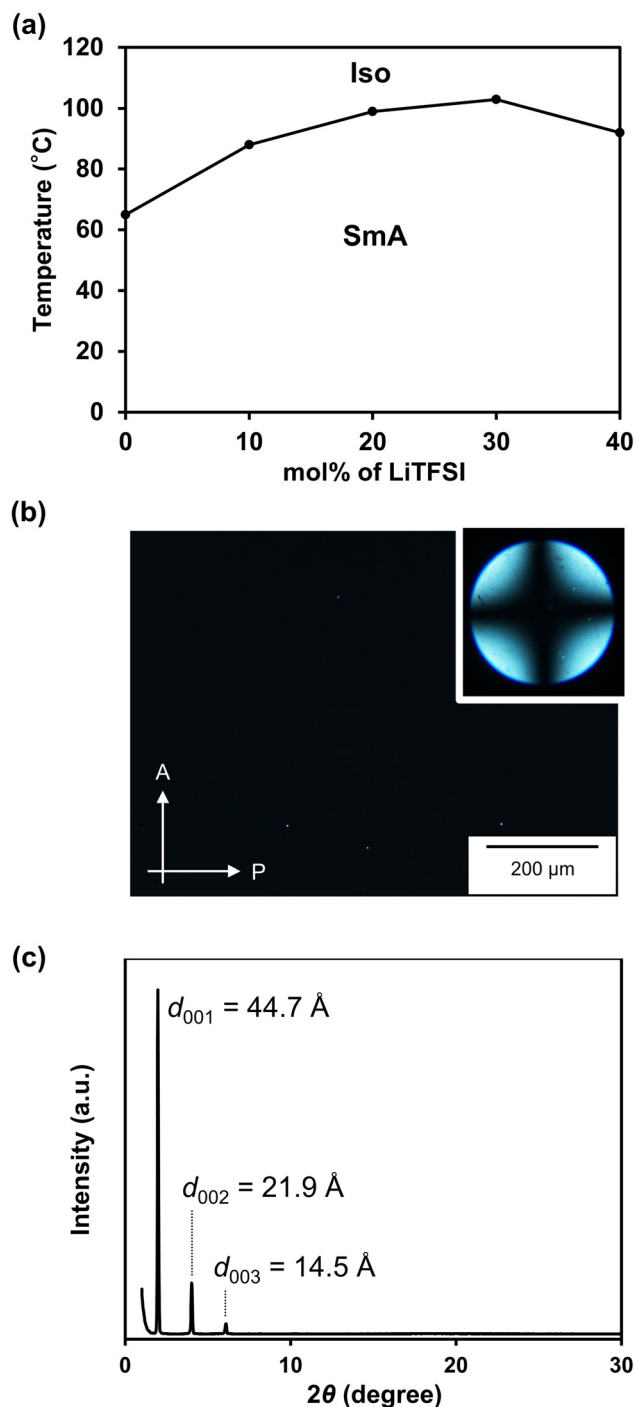
Fig. 5 Schematic illustration of the assembled structure of **1**/LiTFSI at a molar ratio of 80 : 20 in the SmA phase.

Fig. 4 (a) Phase diagram of **1**/LiTFSI complexes upon cooling. Iso: isotropic; SmA: smectic A. (b) POM image of **1**/LiTFSI at a molar ratio of 80 : 20 at 25 °C on glass substrates. A: analyzer. P: polarizer. The inset shows the conoscopic image. (c) XRD pattern of **1**/LiTFSI at a molar ratio of 80 : 20 at 60 °C.

Fig. 6 Ionic conductivities of **1**/LiTFSI at molar ratios of 90 : 10 (orange), 80 : 20 (red), 70 : 30 (green), and 60 : 40 (blue). The right part shows the enlarged view of the region of phase transition temperatures.

comb-shaped gold electrodes deposited on a glass substrate (Fig. 6 and S9†). LC electrolytes **1**/LiTFSI exhibited ionic conductivities of 10^{-6}–10^{-4} S cm^{-1} in the SmA phases. A sudden increase in ionic conductivity was observed in isotropic (Iso)–SmA phase transitions upon cooling of **1**/LiTFSI complexes at
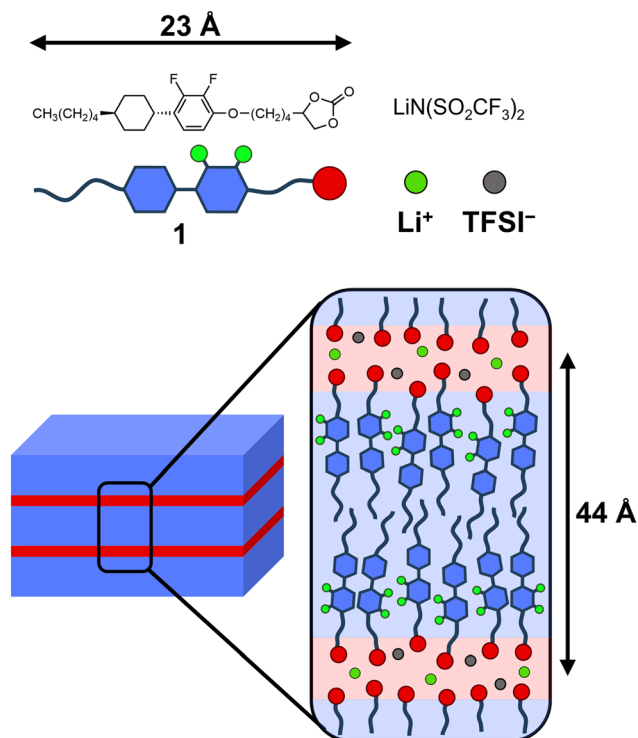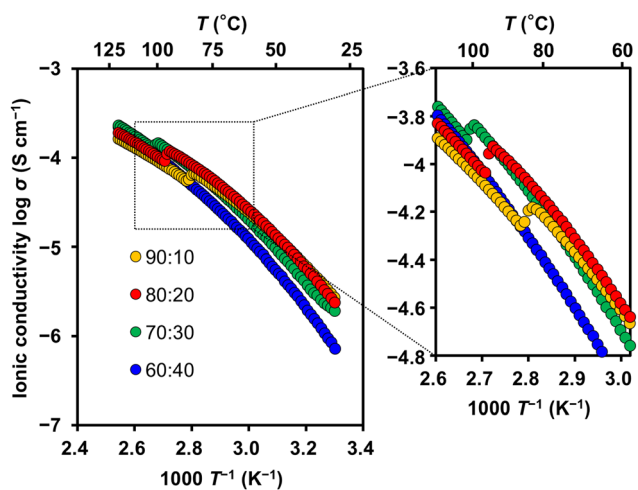
molar ratios of 90 : 10, 80 : 20, and 70 : 30 (Fig. 6). These observations and the XRD results (Fig. 4c) suggest that the formation of aligned 2D pathways leads to more efficient ion transport between the electrodes (Fig. 5). Higher ionic conductivities were obtained for **1**/LiTFSI at molar ratios of 90 : 10 and 80 : 20 than at other ratios. In our previous study,[12] compound **3** was designed to improve the oxidation resistance of compound **2** (Fig. 7). The cyclohexylphenyl mesogen of compound
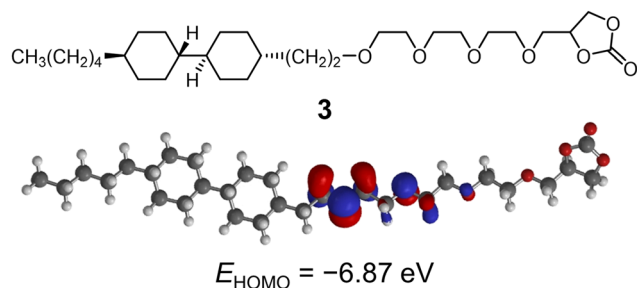
$E_{HOMO} = -6.87$ eV

Fig. 7 Molecular structure, HOMO structure, and the HOMO energy level (DFT, B3LYP/6-31G(d), Spartan'18) of compound **3** bearing a bicyclohexyl mesogen.

2 was changed to the bicyclohexyl mesogen of compound **3**. Flexibility was increased by introducing an oligo(ethylene oxide) spacer. The phase transition temperatures of **1**/LiTFSI and the LC electrolytes based on **2** [11,15] and **3** [12] used for pre-

Table 2 Phase transition behavior of LC electrolytes

LC electrolyte	Phase transition behavior[a]				
1/LiTFSI (80 : 20)	Iso	99	SmA		
2/LiTFSI (90 : 10)[b]	Iso	114	SmA	0	SmB
3/LiTFSI (80 : 20)[c]	Iso	109	SmA	99	SmB

[a] Phase transition temperature (°C) determined by DSC during the cooling process. Scanning rate: 10 °C min⁻¹. [b] Ref. 11 and 15. [c] Ref. 12. Iso: isotropic; SmA: smectic A; and SmB: smectic B.
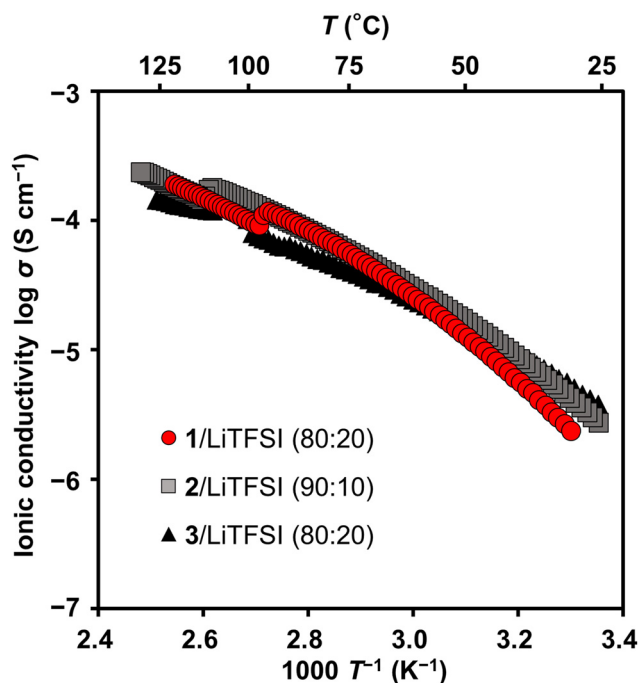

Fig. 8 Comparison of the ionic conductivities of **1**/LiTFSI at an 80 : 20 molar ratio (red circle), **2**/LiTFSI at a 90 : 10 molar ratio[11] (grey square), and **3**/LiTFSI at an 80 : 20 molar ratio[12] (black triangle).

vious lithium-ion battery studies are listed in Table 2. The conductivities of **1**/LiTFSI were compared with those reported in previous studies (Fig. 8).[11,12] The conductivities of **1**/LiTFSI at a molar ratio of 80 : 20 were comparable to those of **2**/LiTFSI[11] and **3**/LiTFSI,[12] suggesting the applicability of **1**/LiTFSI to the electrolytes of lithium-ion batteries. The fluorination of the mesogen did not decrease the ionic conductivities. Comparing ionic conductivities at 60 °C, where lithium-ion batteries with LC electrolytes were operated in our previous report, **1**/LiTFSI at a molar ratio of 80 : 20 showed the highest values among **1**/LiTFSI mixtures. Therefore, **1**/LiTFSI at a molar ratio of 80 : 20
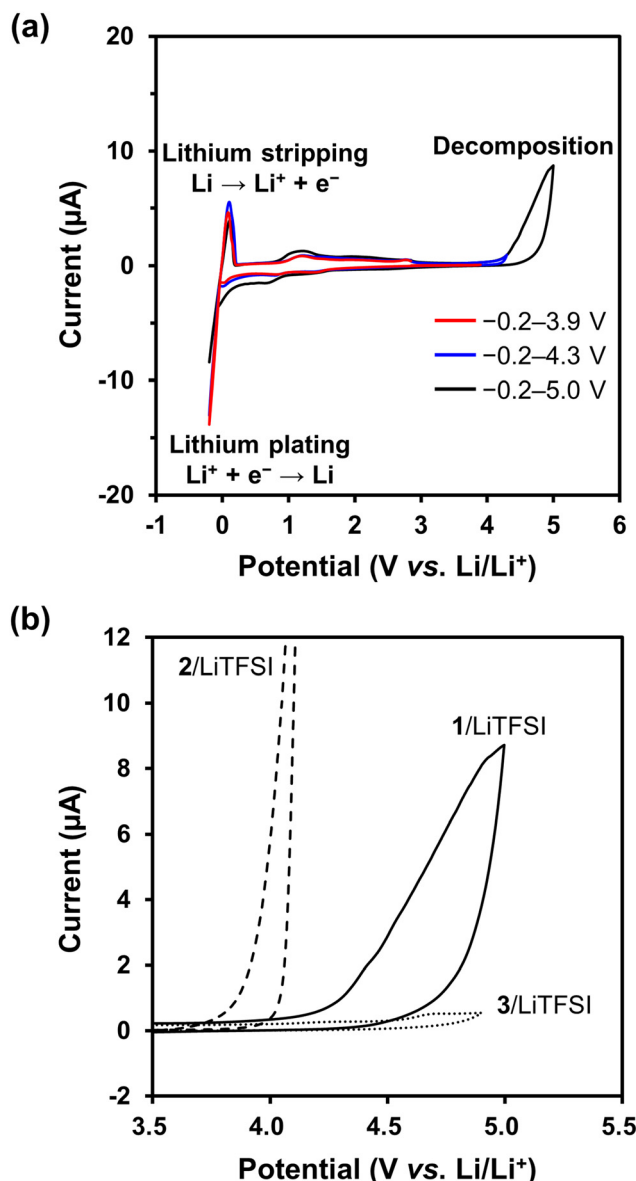

Fig. 9 (a) Cyclic voltammograms of the LC electrolyte **1**/LiTFSI at an 80 : 20 molar ratio in the voltage region of −0.2–3.9 V (red), −0.2–4.3 V (blue), and −0.2–5.0 V (black) vs. Li/Li⁺ at 60 °C. (b) Enlarged CV curves in the high voltage region of **1**/LiTFSI at an 80 : 20 molar ratio (black solid line), **2**/LiTFSI at a 90 : 10 molar ratio[12] (black dashed line), and **3**/LiTFSI at an 80 : 20 molar ratio[12] (black dotted line).

was employed as the LC lithium-ion electrolyte for the following electrochemical measurements.

To evaluate the electrochemical stability of the complex, cyclic voltammetry (CV) of **1**/LiTFSI at a molar ratio of 80 : 20 was performed using a stainless-steel plate as the working electrode and lithium metal as the counter and reference electrodes at 60 °C (Fig. 9). The fluorinated cyclohexylphenyl-based LC electrolyte **1**/LiTFSI was stable in the range from −0.2 V to 4.2 V *vs.* Li/Li$^+$ (Fig. 9a). Considering that **2**/LiTFSI without fluorine substituents on the benzene ring electrochemically decomposed at 4.0 V *vs.* Li/Li$^+$ (Fig. 9b),[12] the fluorination of mesogens was effective for improving the electrochemical stability of LC lithium-ion electrolytes. The electrochemical decomposition of the LC electrolyte **1**/LiTFSI was observed above 4.3 V. The decomposition potential based on the CV measurements of **1**/LiTFSI is seen between those of **2**/LiTFSI and **3**/LiTFSI[12] (Fig. 9b and S10†), which is consistent with the order of the HOMO levels of the respective liquid crystal molecules calculated using DFT (Fig. 2 and 7). These results suggest that the introduction of fluorine substituents reduces the HOMO level and improves oxidation stability. It is known that the electrochemical stability of conventional organic liquid electrolytes can be enhanced by high concentrations of lithium salts.[57,74] To exclude the effect of LiTFSI concentrations on the stability of LC electrolytes, we conducted CV measurement for **1**/LiTFSI at a molar ratio of 90 : 10 (Fig. S11†). The stability of **1**/LiTFSI was comparable with different LiTFSI concentrations, supporting the hypothesis that the fluorination of mesogens enhances oxidation stability.

The performance of lithium-ion batteries based on the LC electrolyte **1**/LiTFSI at a molar ratio of 80 : 20 was studied using half-cells of Li/LC electrolytes/LiFePO$_4$ (Fig. 10 and 11). Fig. 10a shows the charge–discharge curves for the cell based on the **1**/LiTFSI complex in the potential range of 2.5–3.9 V and at a current density of 5 mA g^{-1} for the initial 30 cycles at 60 °C. Half-cells containing the LC electrolyte **1**/LiTFSI exhibited a discharge capacity of 140 mA h g^{-1}, whereas the theoretical capacity of LiFePO$_4$ is 170 mA h g^{-1}. The charge–discharge curves of the cell with **1**/LiTFSI were almost the same
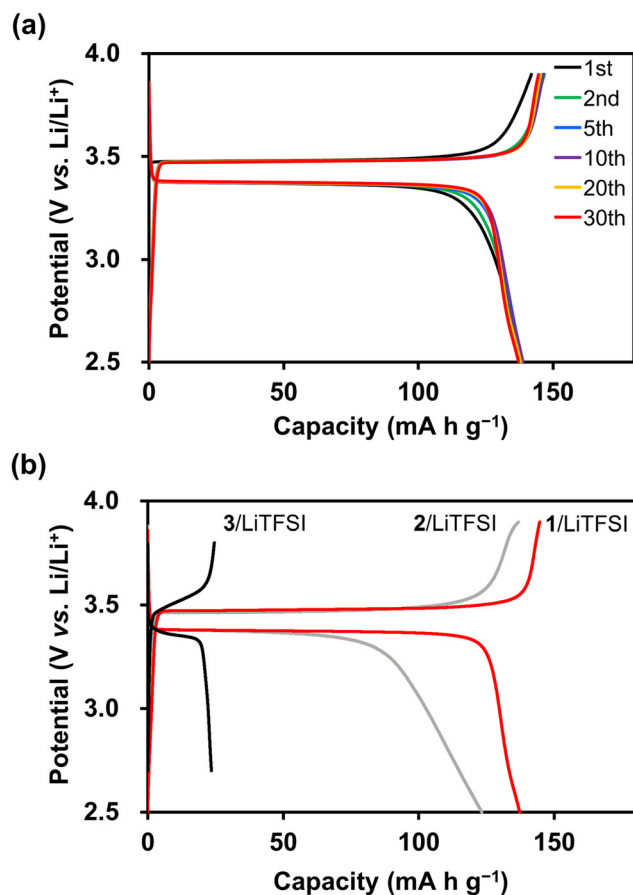

Fig. 10 Charge–discharge curves of half-cells of Li/LC electrolytes/ LiFePO$_4$ using **1**/LiTFSI at an 80 : 20 molar ratio, **2**/LiTFSI at a 90 : 10 molar ratio,[11] and **3**/LiTFSI at an 80 : 20 molar ratio[12] at 60 °C. Potential range: 2.5–3.9 V for **1**/LiTFSI and **2**/LiTFSI, 2.7–3.8 V for **3**/ LiTFSI; current density: 5 mA g^{-1}. (a) Charge–discharge curves of **1**/ LiTFSI for the initial 30 cycles. (b) Representative charge–discharge curves of **1**/LiTFSI (red line), **2**/LiTFSI (grey line), and **3**/LiTFSI (black line) at the 30th cycle.
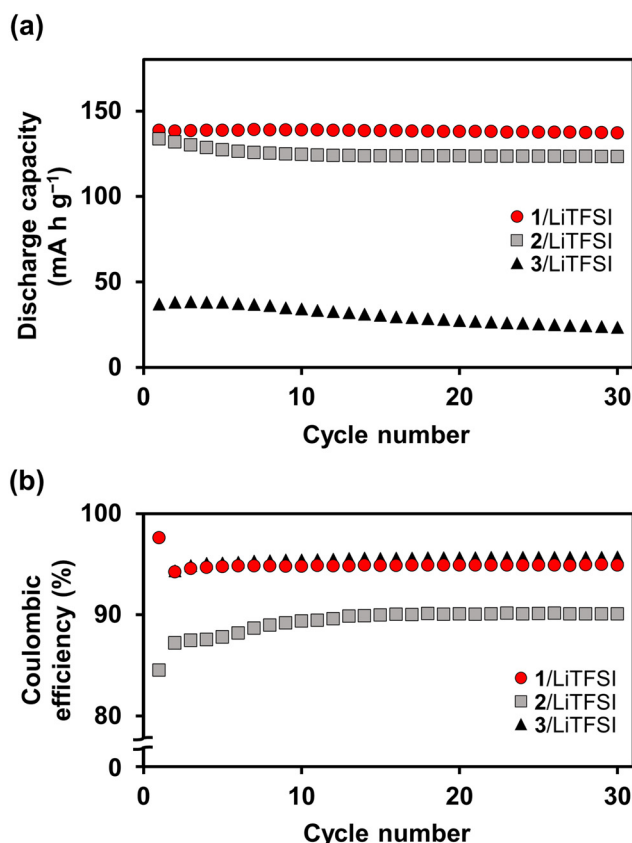

Fig. 11 Cycling performance of half-cells of Li/LC electrolytes/LiFePO$_4$ using **1**/LiTFSI at an 80 : 20 molar ratio (red circle), **2**/LiTFSI at a 90 : 10 molar ratio[11,12] (grey square), and **3**/LiTFSI at an 80 : 20 molar ratio[12] (black triangle) at 60 °C. Potential range: 2.5–3.9 V for **1**/LiTFSI and **2**/LiTFSI, and 2.7–3.8 V for **3**/LiTFSI; current density: 5 mA g^{-1}. (a) Discharge capacity; (b) coulombic efficiency.

within 30 cycles (Fig. 10a). The charge–discharge curves of the cell using **1**/LiTFSI showed small polarization and a clear plateau corresponding to the lithium-ion insertion/extraction of LiFePO$_4$ (Fig. 10b red line), while those for the **2**/LiTFSI cell exhibited greater polarization (Fig. 10b grey line), presumably due to the decomposition of the LC electrolyte. The stable discharge capacities were obtained for the half-cell using **1**/LiTFSI (Fig. 11a). In contrast, the capacity of the half-cell with **2**/LiTFSI[11] gradually decreased, resulting in a lower capacity at the 30th cycle. The coulombic efficiency of the half-cell using **1**/LiTFSI was approximately 95% (Fig. 11b), which was also higher than that of the cell using **2**/LiTFSI. These results show that the fluorination of the mesogen effectively enhances the oxidation resistance of the LC electrolyte to suppress the decomposition of the LC electrolytes during the charge–discharge reactions. The cell using **3**/LiTFSI,[12] which was the most electrochemically stable among **1–3**, also showed a high coulombic efficiency of approximately 95% (Fig. 11b). However, the cell using **3**/LiTFSI showed the smallest capacity among the cells due to the cell resistance resulting from the strong packing of the bicyclohexyl mesogens at an operation temperature of 60 °C (Fig. 11a). Compared to the modification of the molecular framework, the introduction of the fluorine substituents to the mesogenic moieties could enhance the oxidation resistance without inducing closer mesogen packing or significant changes in the LC order, resulting in improved battery performance.
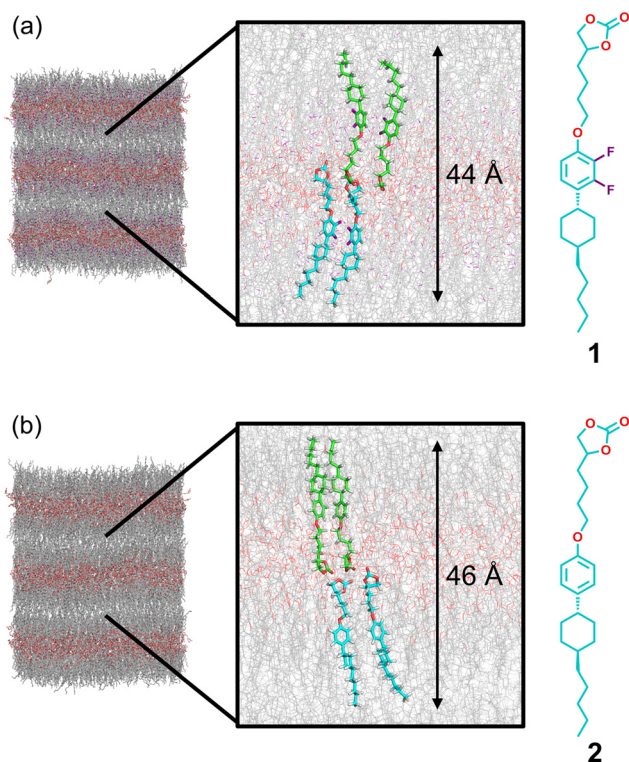
To study the effects of the lateral fluorine groups of the cyclohexylphenyl mesogen on the molecular packing and LC order, molecular dynamics (MD) simulations were performed for compounds **1** and **2** (Fig. 12, 13, and S12–S14†). We recently reported unusual smectic phase transitions of analogous carbonate-based molecules,[75] which were examined using large-scale MD simulations. In the present study, the models and methods of MD simulations[75] were applied to compounds **1** and **2**. The MD simulations of compounds **1** and **2** revealed bilayer structures at 30 °C (Fig. 12). The simulated interlayer distances of compounds **1** (44 Å, Fig. 12a) and **2** (46 Å, Fig. 12b) are consistent with the interlayer distances estimated by the XRD measurements of **1** (43 Å, Fig. S5†) and **2**[11] (46 Å), respectively. The order parameters and electron density profiles of the LC phases of compounds **1** and **2** were calculated from the results of MD simulations (Fig. 13 and S14†). We confirmed that the order parameters of the rigid-rod mesogen and the alkyl spacer of compounds **1** and **2** were almost the same in the SmA phases (Fig. S14†). These results indicated that the LC order of compound **1** was not significantly disrupted by the lateral fluorine groups of the cyclohexylphenyl mesogen. In addition, the high-electron-density region (red region in Fig. 12 left) of compound **1** in the SmA phase was wider than that of compound **2** (Fig. 13).
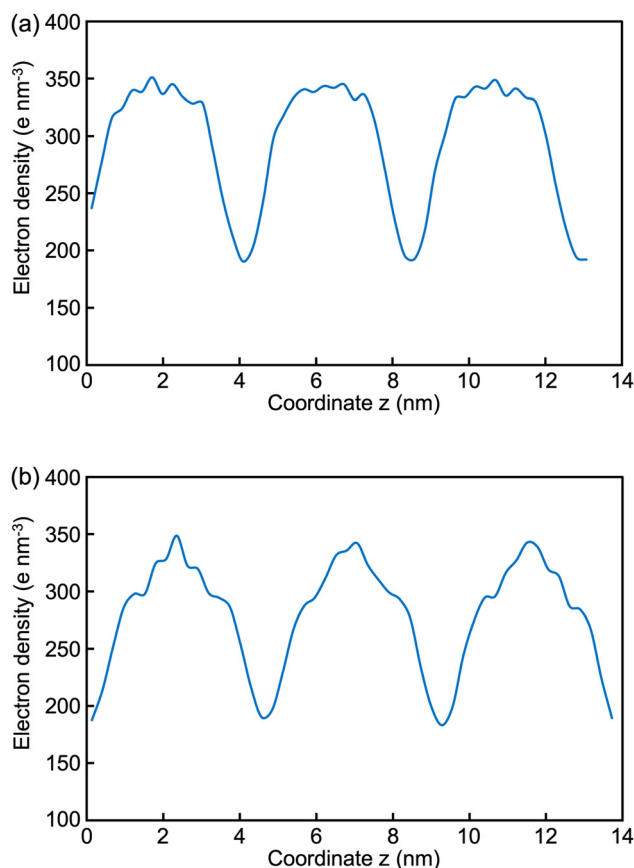

Fig. 12 Side views of MD simulation snapshots after 500 ns of the equilibration run at 30 °C: (a) compound **1** and (b) compound **2**.

Fig. 13 Electron density profiles along the layer normal at 500 ns: (a) compound **1** and (b) compound **2**.

Fluorinated LC molecule **1** exhibits dynamic and ordered 2D ion transport pathways in the SmA phase and improved electrochemical stability. These properties of compound **1** led to higher performances of lithium-ion batteries using LC electrolytes (Fig. 10 and 11).

Conclusions

Nanostructured ion-conductive liquid crystals with high oxidation resistance have been designed based on the approach of mesogen fluorination. Fluorinated LC molecule **1** consisting of cyclohexyl-2,3-difluorophenyl and cyclic carbonate moieties is miscible with LiTFSI, and **1**/LiTFSI complexes exhibit SmA phases over a wide temperature range, including room temperature. The fluorination of the mesogens imparts high oxidation resistance to the LC electrolytes without significantly changing the molecular framework and LC order, resulting in more stable cycling properties and a higher coulombic efficiency of the Li/LC electrolytes/LiFePO$_4$ half-cells. The introduction of fluorine atoms into LC molecules has been used primarily in the field of informational displays to tune the dielectric constant, viscosity, and photophysical properties.[66–71] In the present study, we have demonstrated that this approach can also be applied to liquid crystals for energy devices. The synthesis of electrochemically stable LC molecules *via* fluorination opens up the possibility of their use as LC electrolyte materials in safe and high-performance lithium-ion batteries.

Author contributions

T. K. conceived and designed the study. T. K., J. U., S. T., and K. H. designed the experiments. S. T. and K. H. performed the experiments. S. T. and E. H. performed the cyclic voltammetry and charge–discharge experiments. S. S. and G. W. performed the MD simulations. S. T., K. H., J. U., S. S., G. W., and T. K. wrote the manuscript. All the authors discussed the results and edited the manuscript.

Data availability

The data supporting this article have been included as part of the ESI.†

Conflicts of interest

The authors declare no competing financial interest.

Acknowledgements

References

1 J. Uchida, B. Soberats, M. Gupta and T. Kato, *Adv. Mater.*, 2022, **34**, 2109063.
2 T. Kato, M. Yoshio, T. Ichikawa, B. Soberats, H. Ohno and M. Funahashi, *Nat. Rev. Mater.*, 2017, **2**, 17001.
3 Q. Ruan, M. Yao, D. Yuan, H. Dong, J. Liu, X. Yuan, W. Fang, G. Zhao and H. Zhang, *Nano Energy*, 2023, **106**, 108087.
4 H. K. Bisoyi and Q. Li, *Chem. Rev.*, 2022, **122**, 4887–4926.
5 N. Kapernaum, A. Lange, M. Ebert, M. A. Grunwald, C. Haege, S. Marino, A. Zens, A. Taubert, F. Giesselmann and S. Laschat, *ChemPlusChem*, 2022, **87**, e202100397.
6 T. Kato, M. Gupta, D. Yamaguchi, K. P. Gan and M. Nakayama, *Bull. Chem. Soc. Jpn.*, 2021, **94**, 357–376.
7 W. Pisula and K. Müllen, in *Handbook of Liquid Crystals*, ed. J. W. Goodby, P. J. Collings, T. Kato, C. Tschierske, H. Gleeson and P. Raynes, Wiley-VCH, Weinheim, 2nd edn, 2014, vol. 8, ch. 20, pp. 627–673.
8 M. Kumar and S. Kumar, *Polym. J.*, 2017, **49**, 85–111.
9 J. Kloos, N. Joosten, A. Schenning and K. Nijmeijer, *J. Membr. Sci.*, 2021, **620**, 118849.
10 Y. Shen and I. Dierking, *Appl. Sci.*, 2019, **9**, 2512.
11 J. Sakuda, E. Hosono, M. Yoshio, T. Ichikawa, T. Matsumoto, H. Ohno, H. Zhou and T. Kato, *Adv. Funct. Mater.*, 2015, **25**, 1206–1212.
12 A. Kuwabara, M. Enomoto, E. Hosono, K. Hamaguchi, T. Onuma, S. Kajiyama and T. Kato, *Chem. Sci.*, 2020, **11**, 10631–10637.
13 T. Onuma, E. Hosono, M. Takenouchi, J. Sakuda, S. Kajiyama, M. Yoshio and T. Kato, *ACS Omega*, 2018, **3**, 159–166.
14 T. Onuma, M. Yoshio, M. Obi, K. Kashiwagi, S. Tahara and T. Kato, *Polym. J.*, 2018, **50**, 889–898.
15 Y. Mizumura, D. Högberg, K. Arai, J. Sakuda, B. Soberats, M. Yoshio and T. Kato, *Bull. Chem. Soc. Jpn.*, 2019, **92**, 1226–1233.
16 R. L. Kerr, S. A. Miller, R. K. Shoemaker, B. J. Elliott and D. L. Gin, *J. Am. Chem. Soc.*, 2009, **131**, 15972–15973.
17 A. Eisele, K. Kyriakos, R. Bhandary, M. Schönhoff, C. M. Papadakis and B. Rieger, *J. Mater. Chem. A*, 2015, **3**, 2942–2953.
18 Y. Wang, C. J. Zanelotti, X. Wang, R. Kerr, L. Jin, W. H. Kan, T. J. Dingemans, M. Forsyth and L. A. Madsen, *Nat. Mater.*, 2021, **20**, 1255–1263.
19 Z. Ahmad, Z. Hong and V. Viswanathan, *Proc. Natl. Acad. Sci. U. S. A.*, 2020, **117**, 26672–26680.
20 D. Gopalakrishnan, S. Alkatie, A. Cannon, S. Rajendran, N. K. Thangavel, N. Bhagirath, E. M. Ryan and

L. M. R. Arava, *Sustainable Energy Fuels*, 2021, **5**, 1488–1497.

21 S. Wang, X. Liu, A. Wang, Z. Wang, J. Chen, Q. Zeng, X. Jiang, H. Zhou and L. Zhang, *ACS Appl. Mater. Interfaces*, 2018, **10**, 25273–25284.

22 L. Su, F. Lu, Y. Li, Y. Wang, X. Li, L. Zheng and X. Gao, *ACS Nano*, 2024, **18**, 7633–7643.

23 B. Soberats, M. Yoshio, T. Ichikawa, X. Zeng, H. Ohno, G. Ungar and T. Kato, *J. Am. Chem. Soc.*, 2015, **137**, 13212–13215.

24 T. Kobayashi, Y. Li, A. Ono, X. Zeng and T. Ichikawa, *Chem. Sci.*, 2019, **10**, 6245–6253.

25 S. Chai, F. Xu, R. Zhang, X. Wang, L. Zhai, X. Li, H. J. Qian, L. Wu and H. Li, *J. Am. Chem. Soc.*, 2021, **143**, 21433–21442.

26 B. Soberats, M. Yoshio, T. Ichikawa, S. Taguchi, H. Ohno and T. Kato, *J. Am. Chem. Soc.*, 2013, **135**, 15286–15289.

27 H. Iino, T. Usui and J. Hanna, *Nat. Commun.*, 2015, **6**, 6828.

28 B. X. Dong, Z. Liu, M. Misra, J. Strzalka, J. Niklas, O. G. Poluektov, F. A. Escobedo, C. K. Ober, P. F. Nealey and S. N. Patel, *ACS Nano*, 2019, **13**, 7665–7675.

29 S. Yazaki, M. Funahashi, J. Kagimoto, H. Ohno and T. Kato, *J. Am. Chem. Soc.*, 2010, **132**, 7702–7708.

30 T. Yasuda, H. Ooi, J. Morita, Y. Akama, K. Minoura, M. Funahashi, T. Shimomura and T. Kato, *Adv. Funct. Mater.*, 2009, **19**, 411–419.

31 S. Inoue, K. Nikaido, T. Higashino, S. Arai, M. Tanaka, R. Kumai, S. Tsuzuki, S. Horiuchi, H. Sugiyama, Y. Segawa, K. Takaba, S. Maki-Yonekura, K. Yonekura and T. Hasegawa, *Chem. Mater.*, 2022, **34**, 72–83.

32 T. Kato, J. Uchida, Y. Ishii and G. Watanabe, *Adv. Sci.*, 2024, **11**, 2306529.

33 D. L. Gin, X. Lu, P. R. Nemade, C. S. Pecinovsky, Y. Xu and M. Zhou, *Adv. Funct. Mater.*, 2006, **16**, 865–878.

34 J. Kloos, N. Jansen, M. Houben, A. Casimiro, J. Lub, Z. Borneman, A. P. H. J. Schenning and K. Nijmeijer, *Chem. Mater.*, 2021, **33**, 8323–8333.

35 Y. Zhang, D. Kim, R. Dong, X. Feng and C. O. Osuji, *Sci. Adv.*, 2022, **8**, eabm5899.

36 T. Sakamoto, K. Asakura, N. Kang, R. Kato, M. Liu, T. Hayashi, H. Katayama and T. Kato, *J. Mater. Chem. A*, 2023, **11**, 22178–22186.

37 P. Li, C. Johnson, S. S. Dyer, C. O. Osuji and D. L. Gin, *Adv. Mater. Interfaces*, 2023, **10**, 2201761.

38 D. Kuo, M. Liu, K. R. S. Kumar, K. Hamaguchi, K. P. Gan, T. Sakamoto, T. Ogawa, R. Kato, N. Miyamoto, H. Nada, M. Kimura, M. Henmi, H. Katayama and T. Kato, *Small*, 2020, **16**, 2001721.

39 D. Kuo, T. Sakamoto, S. Torii, M. Liu, H. Katayama and T. Kato, *Polym. J.*, 2022, **54**, 821–825.

40 K. Xu, *Chem. Rev.*, 2004, **104**, 4303–4417.

41 J. Kalhoff, G. G. Eshetu, D. Bresser and S. Passerini, *ChemSusChem*, 2015, **8**, 2154–2175.

42 Y. Chen, Y. Kang, Y. Zhao, L. Wang, J. Liu, Y. Li, Z. Liang, X. He, X. Li, N. Tavajohi and B. Li, *J. Energy Chem.*, 2021, **59**, 83–99.

43 Q. Zhao, S. Stalin, C. Z. Zhao and L. A. Archer, *Nat. Rev. Mater.*, 2020, **5**, 229–252.

44 A. Banerjee, X. Wang, C. Fang, E. A. Wu and Y. S. Meng, *Chem. Rev.*, 2020, **120**, 6878–6933.

45 A. Sakuda, T. Takeuchi and H. Kobayashi, *Solid State Ionics*, 2016, **285**, 112–117.

46 A. Sakuda, A. Hayashi and M. Tatsumisago, *Curr. Opin. Electrochem.*, 2017, **6**, 108–114.

47 Z. Xue, D. He and X. Xie, *J. Mater. Chem. A*, 2015, **3**, 19218–19253.

48 D. Bresser, S. Lyonnard, C. Iojoiu, L. Picard and S. Passerini, *Mol. Syst. Des. Eng.*, 2019, **4**, 779–792.

49 L. Tang, B. Chen, Z. Zhang, C. Ma, J. Chen, Y. Huang, F. Zhang, Q. Dong, G. Xue, D. Chen, C. Hu, S. Li, Z. Liu, Y. Shen, Q. Chen and L. Chen, *Nat. Commun.*, 2023, **14**, 2301.

50 Y. Su, X. Rong, A. Gao, Y. Liu, J. Li, M. Mao, X. Qi, G. Chai, Q. Zhang, L. Suo, L. Gu, H. Li, X. Huang, L. Chen, B. Liu and Y. S. Hu, *Nat. Commun.*, 2022, **13**, 4181.

51 H. Nguyen, G. Kim, J. Shi, E. Paillard, P. Judeinstein, S. Lyonnard, D. Bresser and C. Iojoiu, *Energy Environ. Sci.*, 2018, **11**, 3298–3309.

52 A. Mayer, H. Nguyen, A. Mariani, T. Diemant, S. Lyonnard, C. Iojoiu, S. Passerini and D. Bresser, *ACS Macro Lett.*, 2022, **11**, 982–990.

53 X. Cheng, J. Pan, Y. Zhao, M. Liao and H. Peng, *Adv. Energy Mater.*, 2018, **8**, 1702184.

54 M. Watanabe, M. L. Thomas, S. Zhang, K. Ueno, T. Yasuda and K. Dokko, *Chem. Rev.*, 2017, **117**, 7190–7239.

55 J. Liu, Z. Bao, Y. Cui, E. J. Dufek, J. B. Goodenough, P. Khalifah, Q. Li, B. Y. Liaw, P. Liu, A. Manthiram, Y. S. Meng, V. R. Subramanian, M. F. Toney, V. V. Viswanathan, M. S. Whittingham, J. Xiao, W. Xu, J. Yang, X. Q. Yang and J. G. Zhang, *Nat. Energy*, 2019, **4**, 180–186.

56 W. Li, B. Song and A. Manthiram, *Chem. Soc. Rev.*, 2017, **46**, 3006–3059.

57 K. Yoshida, M. Nakamura, Y. Kazue, N. Tachikawa, S. Tsuzuki, S. Seki, K. Dokko and M. Watanabe, *J. Am. Chem. Soc.*, 2011, **133**, 13121–13129.

58 Y. Wang, Z. Li, Y. Hou, Z. Hao, Q. Zhang, Y. Ni, Y. Lu, Z. Yan, K. Zhang, Q. Zhao, F. Li and J. Chen, *Chem. Soc. Rev.*, 2023, **52**, 2713–2763.

59 N. von Aspern, G. V. Röschenthaler, M. Winter and I. Cekic-Laskovic, *Angew. Chem., Int. Ed.*, 2019, **58**, 15978–16000.

60 Z. Zhang, L. Hu, H. Wu, W. Weng, M. Koh, P. C. Redfern, L. A. Curtiss and K. Amine, *Energy Environ. Sci.*, 2013, **6**, 1806–1810.

61 Y. Sasaki, M. Takehara, S. Watanabe, N. Nanbu and M. Ue, *J. Fluorine Chem.*, 2004, **125**, 1205–1209.

62 Q. Zheng, Y. Yamada, R. Shang, S. Ko, Y.-Y. Lee, K. Kim, E. Nakamura and A. Yamada, *Nat. Energy*, 2020, **5**, 291–298.

63 Z. Yu, H. Wang, X. Kong, W. Huang, Y. Tsao, D. G. Mackanic, K. Wang, X. Wang, W. Huang, S. Choudhury, Y. Zheng, C. V. Amanchukwu, S. T. Hung,

Y. Ma, E. G. Lomeli, J. Qin, Y. Cui and Z. Bao, *Nat. Energy*, 2020, **5**, 526–533.

64 J. Xu, J. Zhang, T. P. Pollard, Q. Li, S. Tan, S. Hou, H. Wan, F. Chen, H. He, E. Hu, K. Xu, X. Yang, O. Borodin and C. Wang, *Nature*, 2023, **614**, 694–700.

65 D. H. C. Wong, J. L. Thelen, Y. Fu, D. Devaux, A. A. Pandya, V. S. Battaglia, N. P. Balsara and J. M. DeSimone, *Proc. Natl. Acad. Sci. U. S. A.*, 2014, **111**, 3327–3331.

66 M. Hird, *Chem. Soc. Rev.*, 2007, **36**, 2070–2095.

67 M. Bremer, P. Kirsch, M. Klasen-Memmer and K. Tarumi, *Angew. Chem., Int. Ed.*, 2013, **52**, 8880–8896.

68 Q. Chen and M. Hird, *Liq. Cryst.*, 2015, **42**, 877–886.

69 G. W. Gray, M. Hird, D. Lacey and K. J. Toyne, *J. Chem. Soc., Perkin Trans. 2*, 1989, 2041–2053.

70 H. F. Gleeson, Y. Wang, S. Watson, D. Sahagun-Sanchez, J. W. Goodby, M. Hird, A. Petrenko and M. A. Osipov, *J. Mater. Chem.*, 2004, **14**, 1480–1485.

71 J. S. Gasowska, S. J. Cowling, M. C. R. Cockett, M. Hird, R. A. Lewis, E. P. Raynes and J. W. Goodby, *J. Mater. Chem.*, 2010, **20**, 299–307.

72 C. Chen, M. Poppe, S. Poppe, C. Tschierske and F. Liu, *Angew. Chem., Int. Ed.*, 2020, **59**, 20820–20825.

73 M. A. Osman, *Mol. Cryst. Liq. Cryst.*, 1985, **128**, 45–63.

74 Y. Yamada, J. Wang, S. Ko, E. Watanabe and A. Yamada, *Nat. Energy*, 2019, **4**, 269–280.

75 K. Hamaguchi, H. Lu, S. Okamura, S. Kajiyama, J. Uchida, S. Sato, G. Watanabe, Y. Ishii, H. Washizu, G. Ungar and T. Kato, *ChemPhysChem*, 2023, **24**, e202200927.